

Reaction-diffusion equations describe heat transfer and flow structure in annular convection

Yuejia Zhang

*NYU-ECNU Institute of Physics and Institute of Mathematical Sciences,
New York University Shanghai, Shanghai, 200124, China*

Nicholas J. Moore*

Department of Mathematics, Colgate University, Hamilton, NY 13346, USA

Jinzi Mac Huang†

*NYU-ECNU Institute of Physics and Institute of Mathematical Sciences,
New York University Shanghai, Shanghai, 200124, China and
Applied Math Lab, Courant Institute, New York University, New York, NY 10012, USA*

(Dated: March 4, 2025)

Heat transfer in a fluid can be greatly enhanced by natural convection, giving rise to the nuanced relationship between the Nusselt number and Rayleigh number that has been a focus of modern fluid dynamics. Our work explores convection in an annular domain, where the geometry reinforces the large-scale circulatory flow pattern that is characteristic of natural convection. The flow must match the no-slip condition at the boundary, leading to a thin boundary layer where both the flow velocity and the temperature vary rapidly. Within such a geometry, a novel Nusselt-Rayleigh scaling emerges, suggesting subtle differences in the heat transfer mechanisms as compared to the well-known case of Rayleigh-Bénard convection. To understand the heat transfer characteristics of this system, we derive a reduced model from the Navier-Stokes-Boussinesq equations where the equations of flow and heat are transformed to a system of low-order partial differential equations (PDEs). This system of PDEs takes the form of a reaction-diffusion system, and its solution preserves the same boundary layer structures seen in the direct numerical simulation (DNS). By matching the solutions inside and outside the boundary layer, our asymptotic analysis recovers the Nusselt-Rayleigh relationship measured in DNS and yields a power-law scaling with exponent $1/4$.

I. INTRODUCTION

Buoyancy variations resulting from the uneven heating of a fluid create a complex motion known as thermal convection. On a planetary scale, thermal convection brings motion to an otherwise motionless world, leading to atmospheric and oceanic flows [1, 2], mantle and liquid-core convection [3–7], solar magneto-hydrodynamics [8], and more [9, 10].

As a relative measure between the buoyancy and viscous forcing, the Rayleigh number Ra dictates the dynamics of thermal convection: Below a critical number $Ra < Ra_1^*$, viscosity damps any motion and the fluid conducts heat as a solid would; At high Ra , convective motion becomes turbulent, leading to dynamical features such as a large-scale circulation (LSC) and enhanced heat transfer [11].

Dimensionlessly, heat transfer is characterized by the Nusselt number, which is the ratio of convective to conductive heat transfer. For $Ra \leq Ra_1^*$, heat transfer is purely conductive, giving $Nu = 1$. For $Ra \gg Ra_1^*$, vigorous convective motion enhances the heat transfer considerably, and a power-law relationship $Nu \propto Ra^\beta$ has been observed in the range from $Ra = 10^6$ to $Ra = 10^{14}$ [12, 13]. The classical scaling of $\beta = 1/3$ can be shown from the boundary layer analysis [14, 15]. In the turbulent regime, the scaling $\beta = 2/7$ is found instead [16]. Recently, a theory developed by Grossmann and Lohse [11, 17, 18] incorporates the heat transfer contributed by both the thermal boundary layers and the bulk mixing, and is found to be consistent with experimental measurements and numerical simulations.

In this limit of high Ra , a large-scale circulation (LSC) can spontaneously develop, whereby the upwelling and downwelling motions combine to form a circulatory flow with overall direction determined by myriad factors such as domain geometry, external forces such as Coriolis, random perturbations, and more. Under certain conditions, the LSC can change its orientation through either a reversal of the circulation direction [19] or a slow migration of the orientation [20]. The development and reversal of LSC have been observed in controlled laboratory experiments [16, 21–29] and numerical simulations [26, 30], leading to many theories exploring its origin and control [19, 24, 31, 32].

* nickmoore83@gmail.com

† machuang@nyu.edu

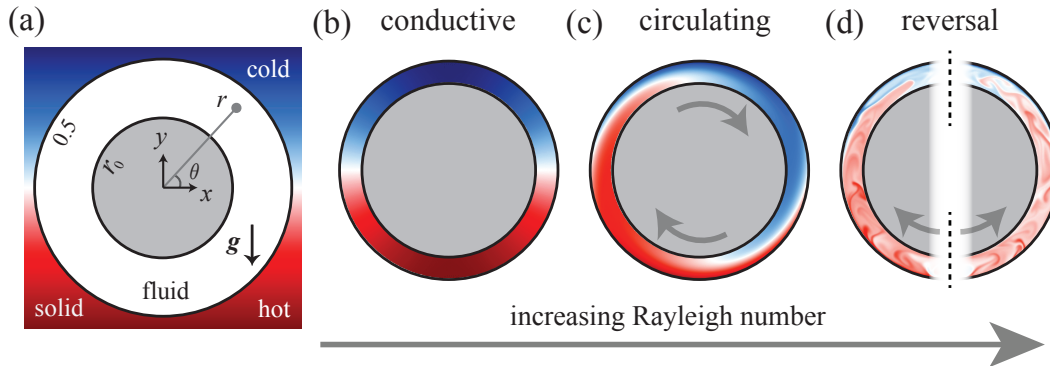


FIG. 1. Thermal convection in an annular domain. (a) The 2-dimensional annular fluid domain $r \in [r_0, \frac{1}{2}]$ is embedded in a solid background with constant vertical temperature gradient. (b) At low Ra , the fluid is motionless and the heat only conducts. (c) Increasing Ra beyond critical, the fluid circulates unidirectionally. (d) Further increasing Ra leads to the reversals of LSC. In (b)-(d), $Pr = 4$ and $r_0 = 0.4$, and the Rayleigh numbers are (b) $Ra = 1.4 \times 10^5$, (c) $Ra = 2.2 \times 10^6$, and (d) $Ra = 1.6 \times 10^9$. Movies of (b)-(d) are included as Supplemental Material.

In [33], LSC dynamics are examined by direct numerical simulations (DNS) in an annular domain of fluid shown in Fig. 1(a). The fluid fills the annulus and is heated from below via a linear temperature profile imposed along the outer ring. As Ra increases, a sequence of dynamical states emerge, including a state of pure conduction [Fig. 1(b)], a state of steady circulation in either the clockwise or counterclockwise direction [Fig. 1(c)], and a state in which the LSC reverses direction spontaneously [Fig. 1(d)]. Numerical simulations of these states are included in Supplemental Material. By exploiting simplifications made possible by the annular geometry, [33] systematically derived a low-dimensional ODE model from the governing Navier-Stokes Boussinesq equations that successfully recovers the range of dynamical states with quantitative accuracy.

While the LSC dynamics have been carefully characterized, the heat transfer properties associated with the annular geometry have received less attention. Interestingly, the nature of heat transfer in an annulus may fundamentally differ from the case of classical Rayleigh-Bénard convection (RBC). In RBC, three mechanisms contribute significantly to heat transfer: thermal boundary layers, circulatory motion, and bulk motion through the center of the domain. In the annulus, however, the inner boundary acts as an obstacle that severely impedes motion through the center. In this way, the annular geometry mitigates the effect of bulk motion, so that circulatory and boundary-layer effects can be examined in isolation. How does Nu scale with Ra in this geometry? Can we derive a model that accurately captures the heat transfer mechanism there? We answer these questions by reducing the Navier-Stokes-Boussinesq equations to a set of low-dimensional PDEs, whose solutions recover the boundary layer structure of the full equations and agree with results obtained from full DNS.

In what follows, we will outline the equations and DNS method in Sec. II, and summarize the previous ODE model in Sec. III. Next, the PDE model of annular convection is introduced in Sec. IV, whose boundary layer analysis is included in Sec. V. Finally, we will show how this PDE model recovers various scalings in Sec. VI, and further discuss these results in Sec. VII.

II. EQUATIONS AND DNS METHOD

The dimensionless Navier-Stokes-Boussinesq equations for velocity \mathbf{u} , pressure p , and temperature T are

$$\frac{\partial \mathbf{u}}{\partial t} + \mathbf{u} \cdot \nabla \mathbf{u} = -\nabla p + Pr \nabla^2 \mathbf{u} + Pr Ra T \mathbf{e}_y, \quad (1)$$

$$\frac{\partial T}{\partial t} + \mathbf{u} \cdot \nabla T = \nabla^2 T, \quad (2)$$

$$\nabla \cdot \mathbf{u} = 0. \quad (3)$$

Here, we have rescaled length by the domain height h , time by the diffusive time scale h^2/κ (κ is the thermal diffusivity), and temperature by the maximum difference ΔT between the top and bottom temperatures imposed on the outer ring. After rescaling, the annular domain of fluid is bounded between radius r_0 and $r_1 = 1/2$ as shown in Fig. 1(a), and the temperature lies in the range $T \in [0, 1]$. Three dimensionless numbers arise: the Rayleigh

number $\text{Ra} = (\beta_T \Delta T h^3 g) / (\nu \kappa)$, the Prandtl number $\text{Pr} = \nu / \kappa$, and the domain aspect ratio $r_0 = R_0 / h$, where β_T is the thermal expansion coefficient, g is the acceleration due to gravity, ν is the kinematic viscosity, and R_0 is the dimensional radius of the inner boundary.

In polar coordinates, $\mathbf{u} = u\mathbf{e}_\theta + v\mathbf{e}_r$ where \mathbf{e}_r and \mathbf{e}_θ are the unit vectors in the r and θ directions, the boundary conditions become

$$u = v = 0 \quad \text{at } r = r_0 \text{ and } r = 1/2, \quad (4)$$

$$\frac{\partial T}{\partial r} = 0 \quad \text{at } r = r_0, \quad (5)$$

$$T = \frac{1 - \sin \theta}{2} \quad \text{at } r = 1/2. \quad (6)$$

We use a pseudo-spectral Chebyshev-Fourier method with implicit-explicit time stepping to solve Eqs. (1) to (3) with boundary conditions Eqs. (4) to (6). In particular, the method recasts Eqs. (1) to (3) in streamfunction-vorticity form [34–36]. The details of our numerical implementation can be found in [33], where second-order convergence in time and spectral accuracy in space were verified.

Without fluid motion ($\mathbf{u} = \mathbf{0}$), it is easy to solve Eq. (2) and obtain the temperature distribution of the conductive state,

$$T_{\text{cond}} = \frac{1}{2} - \frac{1}{r} \left(\frac{r^2 + r_0^2}{1 + 4r_0^2} \right) \sin \theta. \quad (7)$$

We note that this T_{cond} does not balance Eq. (1) and a flow must present near the inner boundary $r = r_0$ due to the Neumann boundary condition Eq. (5). This flow is weak, leading to an $\mathcal{O}(1)$ Reynolds number that is small compared to the flow strength of thermal convection. As this flow has negligible effects on the temperature distribution, we still regard T_{cond} as the conductive state in this study.

With fluid motion, we can define two dimensionless numbers: the Nusselt number measuring the heat transfer rate and the Reynolds number reflecting the flow rate,

$$\text{Nu} = \frac{\langle \int_0^\pi (\partial_r T)|_{r=1/2} d\theta \rangle}{\int_0^\pi (\partial_r T_{\text{cond}})|_{r=1/2} d\theta}, \quad \text{Re} = \text{Pr}^{-1} \langle \max |\mathbf{u}| \rangle, \quad (8)$$

where $\langle \cdot \rangle$ is the long-time average operation. For the Nusselt number, both the convective heat transfer rate (numerator) and the conductive heat transfer rate (denominator) are defined as the rate of heat flowing through the upper half boundary where $r = 1/2$ and $\theta \in (0, \pi)$.

We introduce three coarse-grained variables to describe the heat and flow structures that emerge during annular convection, namely the fluid center of mass (CoM) (X, Y) and the fluid angular momentum L . The angular momentum describes, to leading order, the overall circulatory motion that arises. Meanwhile, (X, Y) quantifies how buoyancy variations alter the CoM. For example, heating the annulus from below, with no flow response, raises the CoM above the annulus center, $Y > 0$, whereas circulatory motion may offset the CoM horizontally. These variables are defined by,

$$X = -\frac{1}{A_0} \int_\Omega r T \cos \theta dA, \quad Y = -\frac{1}{A_0} \int_\Omega r T \sin \theta dA, \quad L = \frac{1}{A_0} \int_\Omega r u dA, \quad (9)$$

where $A_0 = \pi(1 - 4r_0^2)/4$ is the area of the annulus Ω and $dA = r dr d\theta$ is the area element.

III. AN ODE MODEL RECOVERING THE LSC DYNAMICS

Moore & Huang (2024) derived an ODE system from the Navier-Stokes-Boussinesq equations that describes the evolution of the coarse-grained variables X , Y , and L [33]. Here, we briefly sketch the derivation of the ODE system in a way that will generalize to the new PDE model.

To begin, we expand each of the temperature T and the flow velocity $\mathbf{u} = u\mathbf{e}_\theta + v\mathbf{e}_r$ fields as a Fourier series in θ ,

$$T(r, \theta, t) = a_0(r, t) + \sum_{n=1}^{\infty} a_n(r, t) \cos n\theta + b_n(r, t) \sin n\theta, \quad (10)$$

$$u(r, \theta, t) = \sum_{n=-\infty}^{\infty} u_n(r, t) e^{in\theta}, \quad v(r, \theta, t) = \sum_{n=-\infty}^{\infty} v_n(r, t) e^{in\theta}. \quad (11)$$

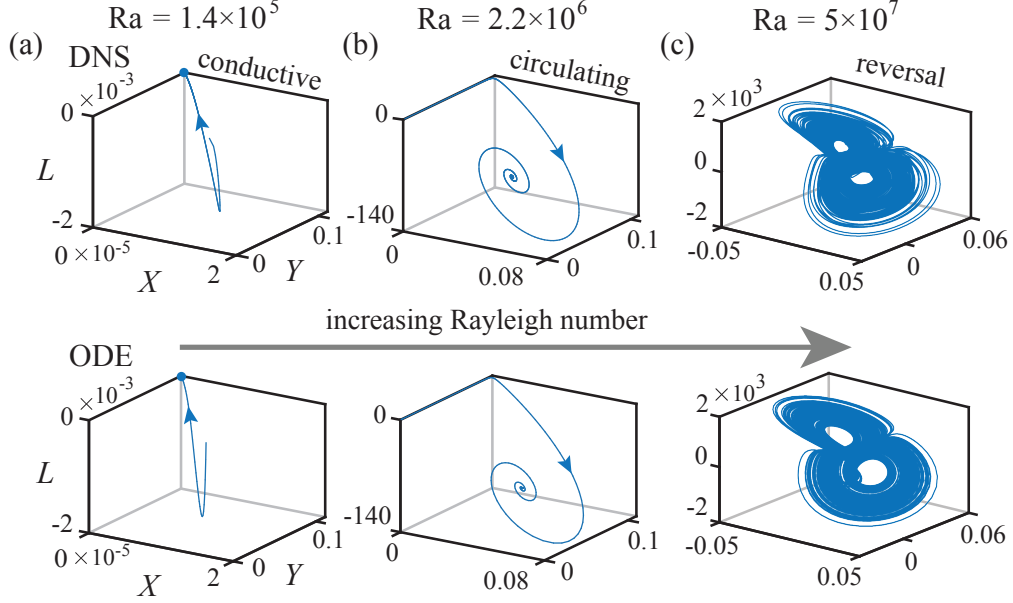


FIG. 2. Trajectories of (L, X, Y) obtained from the DNS result and the ODE model. (a) Conductive state at $Ra = 1.4 \times 10^5$. (b) Circulating state at $Ra = 2.2 \times 10^6$. (c) Reversal state at $Ra = 5 \times 10^7$. In all simulations, $Pr = 4$ and $r_0 = 0.4$.

In the thin channel limit $r_0 \rightarrow 1/2$, the dominant balance of Eqs. (3) and (4) implies $v \rightarrow 0$ and $\partial_\theta u \rightarrow 0$, giving $u = u_0(r, t)$ and $v = 0$ at leading order. Making these substitutions and integrating the u component of Navier-Stokes Eq. (1) over θ gives

$$r^2 \frac{\partial u_0}{\partial t} = \frac{r^2}{2} Pr \cdot Ra \cdot a_1 + Pr \left[-u_0 + r \frac{\partial}{\partial r} \left(r \frac{\partial u_0}{\partial r} \right) \right]. \quad (12)$$

Meanwhile, inserting the truncation $u = u_0(r, t)$ into Eq. (2) decouples the temperature modes,

$$r^2 \dot{a}_n = -nr u_0(r, t) b_n - n^2 a_n + r \partial_r (r \partial_r a_n), \quad (13)$$

$$r^2 \dot{b}_n = +nr u_0(r, t) a_n - n^2 b_n + r \partial_r (r \partial_r b_n). \quad (14)$$

This equation holds for $n = 0, 1, 2, \dots$.

The boundary conditions for Eqs. (12) to (14) are

$$u_0 = \partial_r a_n = \partial_r b_n = 0 \quad \text{at } r = r_0, \quad (15)$$

$$u_0 = 0, a_0 = 1/2, b_1 = -1/2, \text{ all others vanish} \quad \text{at } r = 1/2. \quad (16)$$

for $n = 0, 1, 2, \dots$.

By representing u_0 , a_1 , and b_1 each as a truncated Laurent series in r and inserting into Eqs. (12) to (14), Moore & Huang (2024) obtained the following dynamical system for the evolution of (L, X, Y) [33]:

$$\dot{L} = -Ra Pr X - \alpha Pr L, \quad (17)$$

$$\dot{X} = -kL(Y - y_1) - \beta X, \quad (18)$$

$$\dot{Y} = +kLX - \beta(Y - y_0), \quad (19)$$

where $\alpha, \beta, k, y_0, y_1$ are non-negative coefficients that depend on geometry alone (i.e. independent of Ra and Pr).

Linear stability analysis of Eqs. (17) to (19) reveals two critical Rayleigh numbers: Ra_1^* marks the loss of stability of the conductive state and the simultaneous emergence of the (bistable) circulating states, while Ra_2^* marks the loss of stability of the circulating state and the subsequent onset of LSC reversals [33]. Exact formulas for Ra_1^* and Ra_2^* are provided in [33]. To briefly demonstrate the transitions, Fig. 2 shows trajectories of $(L(t), X(t), Y(t))$ computed from the DNS (top) and from the ODE system (bottom) for three Rayleigh numbers. In this figure, the parameters $Pr = 4$ and $r_0 = 0.4$ are fixed, yielding $Ra_1^* = 7.3 \times 10^5$ and $Ra_2^* = 1.6 \times 10^7$. Figure 2(a) shows the case $Ra < Ra_1^*$, giving

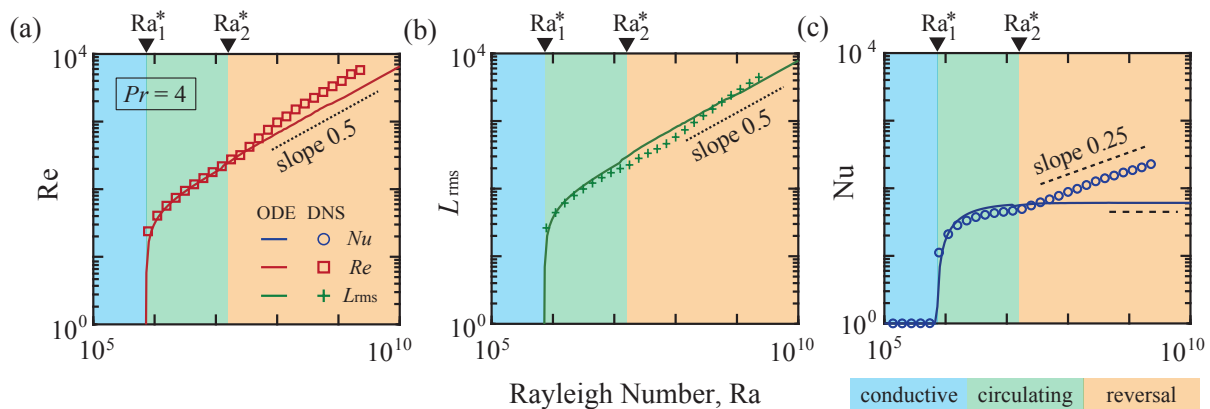


FIG. 3. Re , L_{rms} , Nu measured from the DNS and the ODE model. Reynolds number (a) and fluid angular momentum (b) are zero when $Ra < Ra_1^*$ but have a 0.5 power-law scaling at high Ra . Both the DNS (symbols) and the ODE (curves) solutions capture this scaling. (c) Nusselt number is unity for the conductive state $Ra < Ra_1^*$ and has a 0.25 power-law scaling for high Ra . In this limit, the ODE model approaches a constant Nu , thus it fails to capture the heat transfer of annular convection. In all simulations, $Pr = 4$ and $r_0 = 0.4$, and two critical Rayleigh numbers are identified as $Ra_1^* = 7.3 \times 10^5$ and $Ra_2^* = 1.6 \times 10^7$.

convergence to the stable conductive state in both DNS and the ODE model. Figure 2(b) features the intermediate case, $Ra_1^* < Ra < Ra_2^*$, resulting in convergence to steady circulation. Figure 2(c) shows the high Rayleigh number case, $Ra_2^* < Ra$, which gives chaotic LSC reversals in both the DNS and ODE system. More detailed discussion of these transitions can be found in [33].

While Fig. 2 shows that the ODE model captures the trajectories of $(L(t), X(t), Y(t))$ with surprising detail, we now evaluate other features of the model, including those that quantify the heat transport. We focus on the coarse-grained variables Nu and Re , defined in Eq. (8). In the DNS, these quantities are computed directly from Eq. (8). We also compute the root-mean-square average of angular momentum, $L_{\text{rms}} = \sqrt{\langle L^2 \rangle}$, which reflects the overall strength of the LSC. For the ODE model, insertion of the truncated fields $u = u_0(r, t)$ and $T = 1/2 + a_1(r, t) \cos \theta + b_1(r, t) \sin \theta$ into Eq. (8) yields the formulas

$$Re = \frac{12}{Pr} \left(\frac{1 - \sqrt{2r_0}}{1 + \sqrt{2r_0}} \right) L_{\text{rms}}, \quad (20)$$

$$Nu = \frac{48(1 + 2r_0)(1 + 4r_0^2)}{(1 - 2r_0)^2(1 + 6r_0 + 16r_0^2)} \left[\frac{1 + 2r_0 + 4r_0^2}{12(1 + 2r_0)} - \langle Y \rangle \right]. \quad (21)$$

where $\langle Y \rangle$ is the mean height of the fluid CoM. Physically speaking, vigorous convection both intensifies thermal transport and lowers the fluid CoM by allowing warm fluid to rise more easily. As such, $\langle Y \rangle$ and Nu are negatively related, as borne out by Eq. (21).

Figure 3 shows the three coarse-grained quantities, Re , L_{rms} , and Nu , plotted against Ra for both the DNS (symbols) and the ODE model (curves). The Reynolds number and LSC strength in Fig. 3(a)-(b) show good agreement between the ODE and the DNS: For $Ra < Ra_1^*$, there is no fluid motion so both Re and L_{rms} vanish; For high Ra , a common power law with exponent 0.5 exists as Eq. (20) indicates that Re and L_{rms} are proportional to each other. The scaling $Re \sim Ra^{0.5}$ is also present in the classic RBC [11], and we will later verify this scaling through a dominant-balance analysis.

Figure 3(c) shows the heat transfer rate as quantified by the Nusselt number, Nu . Below the threshold $Ra < Ra_1^*$, Nu is identically one as heat transfer is purely conductive. For $Ra > Ra_1^*$, Nu increases with Ra as convective motion sets in and then grows in strength. The ODE model predicts the Nu - Ra behavior reasonably well in the range $Ra_1^* < Ra < Ra_2^*$, but for $Ra > Ra_2^*$ there is considerable discrepancy. The DNS shows that Nu continues to grow as Ra increases, with the measured data points suggesting the power law $Nu \sim Ra^{0.25}$. The ODE model, however, predicts Nu to saturate to a constant value at large Ra . In fact, [33] shows that the value of $\langle Y \rangle$ predicted by the ODE-model becomes independent of Ra if Ra is sufficiently large, which through Eq. (21) implies the horizontal asymptote of Nu seen in Fig. 3(c). This discrepancy in the behavior of Nu suggests that the ODE model may have oversimplified the temperature field by neglecting fine-scale structure in thermal gradients. To address this deficiency, we next present a PDE model that accurately resolves the thermal boundary layer structure of annular convection.

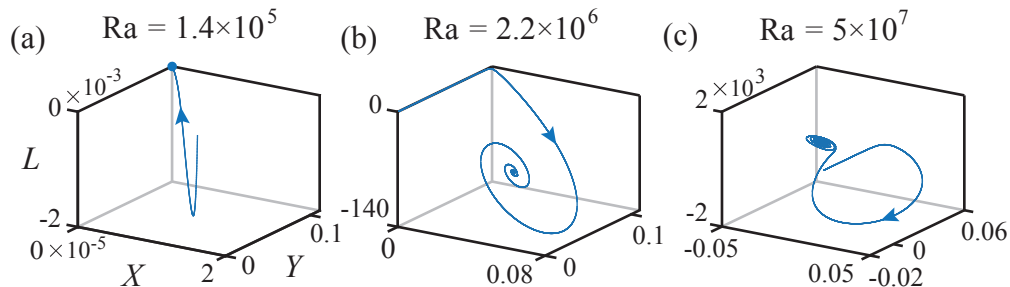


FIG. 4. Trajectories of (L, X, Y) obtained from the PDE model. (a) Conductive state at $Ra = 1.4 \times 10^5$. (b) Circulating state at $Ra = 2.2 \times 10^6$. (c) At $Ra = 5 \times 10^7$, the PDE solution converges to a circulating state instead of a chaotic reversal state. In all simulations, $Pr = 4$ and $r_0 = 0.4$.

IV. REACTION-DIFFUSION PDE MODEL

Rather than expanding the r -dependence of the main state variables in a Laurent series, we observe that truncating Eqs. (12) to (14) at the first Fourier mode in θ and retaining the full dependence on r produces a closed PDE system,

$$\frac{\partial u_0}{\partial t} = \frac{1}{2} Pr \cdot Ra \cdot a_1 + \frac{Pr}{r^2} \left[-u_0 + r \frac{\partial}{\partial r} \left(r \frac{\partial u_0}{\partial r} \right) \right]. \quad (22)$$

$$\frac{\partial a_1}{\partial t} = -\frac{u_0 b_1}{r} + \frac{1}{r^2} \left[-a_1 + r \frac{\partial}{\partial r} \left(r \frac{\partial a_1}{\partial r} \right) \right], \quad (23)$$

$$\frac{\partial b_1}{\partial t} = +\frac{u_0 a_1}{r} + \frac{1}{r^2} \left[-b_1 + r \frac{\partial}{\partial r} \left(r \frac{\partial b_1}{\partial r} \right) \right], \quad (24)$$

Equations (15) and (16) give boundary conditions,

$$u_0 = 0, \quad \partial_r a_1 = 0, \quad \partial_r b_1 = 0 \quad \text{at } r = r_0, \quad (25)$$

$$u_0 = 0, \quad a_1 = 0, \quad b_1 = -1/2 \quad \text{at } r = 1/2. \quad (26)$$

Interestingly, the above PDE system is a *reaction-diffusion* system. This system can be solved by standard numerical methods [34, 37]. In particular, we use a pseudo-spectral Chebyshev-Fourier method to discretize $u_0(r, t)$, $a_1(r, t)$, $b_1(r, t)$ in space and an implicit-explicit method to step forward in time [33].

From the numerical solution of Eqs. (22) to (26), we can compute the quantities $L(t)$, $X(t)$, and $Y(t)$ via Eq. (9). Figure 4 shows the trajectories of (L, X, Y) at the same three values of Ra used in Fig. 2. Figure 4(a)-(b) shows that the new PDE system accurately recovers the dynamics in the conductive (a) and the circulating (b) regimes, agreeing with both the ODE model and the full DNS. We see in Fig. 4(c), however, that the new PDE system fails to predict chaotic LSC reversals. Instead, the numerical solutions exhibit a single reversal and then convergence to a circulating state. It appears the damping effect of diffusion in Eqs. (22) to (24) overcomes what would otherwise be chaotic dynamics. This situation results from the choice to fully resolve the r -dependency while leaving θ -dependency truncated to the lowest order in Eqs. (22) to (24). Despite this weakness in predicting coarse-grained *dynamics*, we will see the PDE model considerably improves the prediction of *time-averaged thermal transport* as quantified by Nu .

Seeing as the numerical solutions of Eqs. (22) to (26) always exhibit convergence to a steady state, regardless of the Ra value, we hereafter focus on the steady-state quantities $a_1 = a_1(r)$, $b_1 = b_1(r)$, and $u_0 = u_0(r)$. Figure 5 provides a visualization of these steady-state solutions at three different Rayleigh numbers. The bottom row shows the profiles $a_1(r)$, $b_1(r)$, and $u_0(r)$ directly, while the top row shows the corresponding temperature and velocity fields computed via $T = 1/2 + a_1(r) \cos \theta + b_1(r) \sin \theta$ and $u = u_0(r)$. In the first case of $Ra < Ra_1^*$ [Fig. 5(a) and (d)], the conductive state $a_1 = 0, b_1 = -(r + r_0^2 r^{-1}) / (1 + 4r_0^2), u_0 = 0$ corresponding to Eq. (7) is stable and there is no fluid motion. Increasing Ra beyond Ra_1^* gives rise to the circulating state with nontrivial flow field, as first seen in Fig. 5(b) and (e). At even higher Rayleigh number, Figs. 5(c) and (f) show that a circulating state still emerges as a steady state, but, interestingly, the profiles show a distinct boundary-layer structure. That is, sharp temperature and flow variations appear only in a narrow region surrounding the outer boundary $r = 1/2$, where the thermal forcing is imposed. As seen in the next section, this emergent boundary-layer structure leads to accurate predictions of the thermal transport, despite the absence of reversal dynamics in the PDE model.

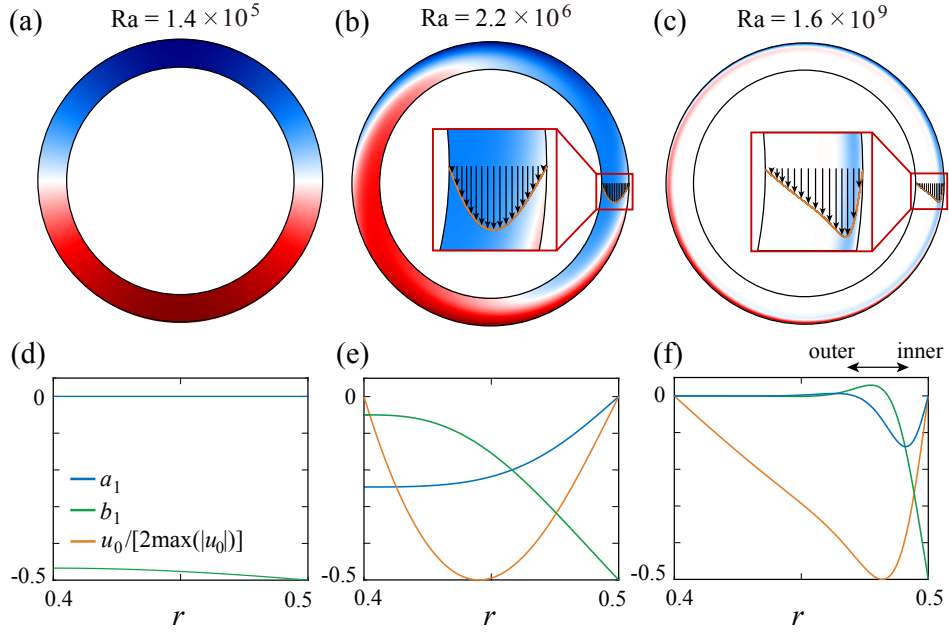


FIG. 5. Steady-state PDE solutions of the flow and temperature fields. (a)-(c) show the PDE solutions with increasing Ra . Thermal and momentum boundary layers develop at high Ra as shown in the zoom-in view (inset) of (c). (d)-(f) show the distribution of a_1 , b_1 , and u_0 corresponding to (a)-(c). In all simulations, $Pr = 4$ and $r_0 = 0.4$.

V. BOUNDARY LAYER ANALYSIS OF THE PDE MODEL

With the aim of predicting thermal transport, we now conduct boundary-layer analysis of the reaction-diffusion PDE system Eqs. (22) to (26) in the limit of high Ra . The characteristic boundary layer thickness $\delta \ll 1$, marks the so-called inner region near $r = 1/2$ where sharp temperature and flow variations dominate; see Fig. 5(c) and (f). We first analyze this region by introducing the stretched coordinate $R = (1/2 - r)/\delta$. Rewriting Eqs. (22) to (24) in terms of variables $A(R) = a_1(r(R))$, $B(R) = b_1(r(R))$, and $U(R) = u_0(r(R))$ gives

$$\delta^{-2} A'' + \frac{2\delta^{-1}}{1-2R\delta} A' + \frac{4}{(1-2R\delta)^2} A = \frac{2}{1-2R\delta} UB, \quad (27)$$

$$\delta^{-2} B'' + \frac{2\delta^{-1}}{1-2R\delta} B' + \frac{4}{(1-2R\delta)^2} B = -\frac{2}{1-2R\delta} UA, \quad (28)$$

$$\delta^{-2} U'' + \frac{2\delta^{-1}}{1-2R\delta} U' + \frac{4}{(1-2R\delta)^2} U = -\frac{1}{2} Ra A, \quad (29)$$

Since $\delta \ll 1$, the first term on each left-hand side (with prefactor δ^{-2}) dominates the second and third terms. The only possible non-trivial balance as $\delta \rightarrow 0$ is therefore

$$\delta^{-2} A'' = 2 UB, \quad \delta^{-2} B'' = -2 UA, \quad \delta^{-2} U'' = -\frac{1}{2} Ra A. \quad (30)$$

Meanwhile, Eqs. (25) and (26) imply boundary conditions

$$U(0) = A(0) = 0, \quad B(0) = -1/2. \quad (31)$$

Far-field ($R \rightarrow \infty$) conditions on U, A, B would be obtained by matching to the outer solution.

The nonlinear system of ODEs given by Eq. (30) does not appear to be amenable to exact solution and so we consider asymptotic behavior for $Ra \gg 1$. Assuming scaling relationships $A = \mathcal{O}(Ra^\mu)$, $B = \mathcal{O}(Ra^\nu)$, $U = \mathcal{O}(Ra^\lambda)$, $\delta = \mathcal{O}(Ra^\epsilon)$ and inserting into Eq. (30) yields the three algebraic equations,

$$\mu = \nu, \quad \lambda = -2\epsilon, \quad -4\epsilon = 1 + \mu. \quad (32)$$

Since there are four unknown exponents, this system is under-determined.

A fourth condition arises from knowledge of the steady-state Fourier coefficients A and B . Due to Eqs. (2) and (3), the steady-state temperature field $\lim_{t \rightarrow \infty} T(r, \theta, t)$ satisfies a maximum principle. In particular, it is limited by the values from Eq. (6) imposed on the Dirichlet boundary, $0 \leq \lim_{t \rightarrow \infty} T(r, \theta, t) \leq 1$. We remark that this bound does not hold for finite time because the initial temperature distribution may have values outside of the range $[0, 1]$. Nonetheless, the bound on the steady-state temperature field implies that the magnitude of the Fourier coefficients A and B are bounded above, independent of Ra . Therefore, these variables are at most $\mathcal{O}(1)$ with respect to $\text{Ra} \gg 1$, giving $\mu, \nu \leq 0$. Further, the condition $B(0) = -1/2$ from Eq. (31) implies that $\nu = 0$. With this extra piece of information, the unique solution to Eq. (32) is $\nu = 0$, $\mu = 0$, $\lambda = 1/2$, $\epsilon = -1/4$, which gives the following scaling relations for $\text{Ra} \gg 1$,

$$A = \mathcal{O}(1), B = \mathcal{O}(1), U = \mathcal{O}(\text{Ra}^{1/2}), \delta = \mathcal{O}(\text{Ra}^{-1/4}). \quad (33)$$

In particular, the scaling of the boundary layer thickness $\delta = \mathcal{O}(\text{Ra}^{-1/4})$, along with $A, B = \mathcal{O}(1)$, gives an estimate of the boundary heat flux, $\partial_r T|_{r=1/2} = \mathcal{O}(\delta^{-1}) = \mathcal{O}(\text{Ra}^{1/4})$, which, through definition Eq. (8), implies the following scaling law for the Nusselt number,

$$\text{Nu} \propto \text{Ra}^{1/4} \quad \text{for } \text{Ra} \gg 1. \quad (34)$$

We next consider the outer region in which r is sufficiently separated from the boundary $r = 1/2$. In this region, the flow velocity u_0 must match U as $r \rightarrow 1/2$, giving $u_0 = \mathcal{O}(\text{Ra}^{1/2})$. Recall that a_1, b_1 are bounded in magnitude by the maximum principle. Inserting the scaling $u_0 = \mathcal{O}(\text{Ra}^{1/2})$ into Eqs. (23) and (24), the variables a_1 and b_1 must be (strictly) asymptotically smaller than $\mathcal{O}(\text{Ra}^{-1/2})$ in order to avoid a contradiction; that is, $a_1, b_1 = o(\text{Ra}^{-1/2})$. Inserting this information into Eq. (22) gives a variable-coefficient ODE satisfied by u_0 ,

$$r \frac{\partial}{\partial r} \left(r \frac{\partial u_0}{\partial r} \right) - u_0 = 0 \quad (35)$$

The solution that satisfies the correct matching condition is $u_0 = \text{Ra}^{1/2} C(r - r_0^2/r)$ where C is an $\mathcal{O}(1)$ constant that would in principle be determined by the matching procedure. Figure 5(f) provides numerical confirmation of the asymptotic shape of the flow profile u_0 as well as the fact that $a_1, b_1 \rightarrow 0$ as $\text{Ra} \rightarrow \infty$.

An immediate consequence of this analysis is that the characteristic flow speed U increases as the square root of the Rayleigh number, as is consistent with the classic RBC results [11]. Furthermore, inserting the scaling of U into the definitions Eq. (8) gives the scaling laws

$$\text{Re} \propto \text{Pr}^{-1} \text{Ra}^{1/2}, \quad L_{\text{rms}} \propto \text{Ra}^{1/2}, \quad (36)$$

which, along with Eq. (34), can be tested against DNS.

VI. RESULTS

We now aim to test the predictions offered by the reduced PDE model, Eqs. (22) to (24), especially scaling laws Eqs. (34) and (36) that result from boundary-layer analysis of the model. As previously discussed, the reduced PDE model does not accurately describe temporally sensitive features, such as LSC reversal events. Nonetheless, it may offer improved predictions for time-averaged quantities, such as thermal transport, due to its ability to resolve small boundary layers in r . Accordingly, Fig. 6 shows measurements of three time-averaged quantities: $\text{Re} \cdot \text{Pr}$, L_{rms} , and Nu . The figure shows these values as measured in DNS of the full Navier-Stokes-Boussinesq equations (symbols), as well as those computed from numerically solving the reduced PDE model (solid curves). As seen in the figure, results from DNS and from the PDE model agree closely with one another for all Ra shown, with only slight discrepancies between the two visible. In particular, Fig. 6(a) shows that the product $\text{Re} \cdot \text{Pr}$ collapses all of the data from different Pr simulations onto a single master curve, which is indeed well predicted by the PDE model. Figure 6(b) confirms that the PDE model also recovers the mean angular momentum accurately. Further, the scaling law Eq. (36), predicts both $\text{Re} \cdot \text{Pr}$ and Pr to scale as $\text{Ra}^{1/2}$, as confirmed by comparison with the dotted line.

The most important question now becomes whether the new PDE model accurately predicts thermal transport as this was the shortcoming of the ODE model of [33]. Accordingly, Figure 6(c) shows measurements of the Nusselt number from the DNS (data points), the new PDE model (solid curve), and the scaling law $\text{Nu} \propto \text{Ra}^{1/4}$ obtained from boundary layer analysis. The figure confirms that the PDE model accurately predicts the Nu computed in the

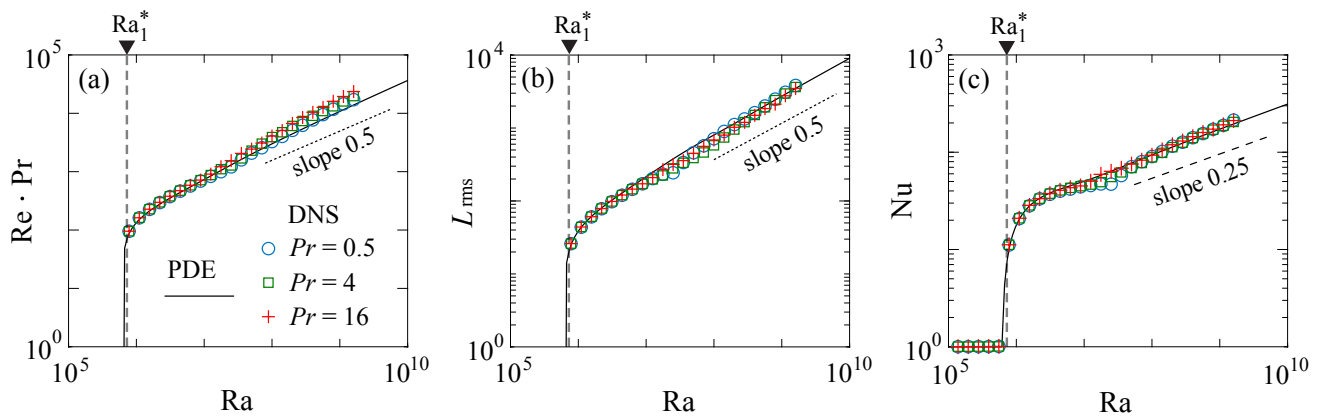


FIG. 6. Re , L_{rms} , and Nu obtained from the DNS (symbols) and PDE (curves) solutions. (a) The Reynolds number has a scaling $Re \propto Pr^{-1}Ra^{1/2}$. (b) Fluid angular momentum scales as $L_{rms} \propto Ra^{1/2}$. (c) Nusselt number has a 1/4 power-law, $Nu \propto Ra^{1/4}$. Here $r_0 = 0.4$, leading to $Ra_1^* = 7.3 \times 10^5$.

full DNS for all three Prandtl numbers tested. Both the PDE model and DNS show that Nu is unity for $Ra < Ra_1$ and then rises sharply for $Ra > Ra_1$ as thermal convection sets in and strongly enhances thermal transport. The discrepancies between the PDE model and DNS are relatively small, on the order of 5-20%, over 4 decades of Ra and 1.5 decades of Pr . This level of accuracy is perhaps better than expected considering that the PDE model only resolves the lowest non-trivial modes, $u_0(r, t)$, $a_1(r, t)$, $b_1(r, t)$, in the θ variable. The agreement therefore suggests that these lowest θ -modes are the ones most responsible for thermal transport, and that the long-time thermal transport is relatively insensitive to dynamic features such as LSC reversals.

Furthermore, Fig. 6(c) shows that, for large values of Ra , both the PDE model and the full DNS closely follow the $Nu \propto Ra^{1/4}$ power law, Eq. (34), that arises from boundary layer analysis. This agreement suggests that convective thermal transport in the annulus primarily arises from the boundary-layer structure of the lowest Fourier modes, $u_0(r, t)$, $a_1(r, t)$, $b_1(r, t)$, near the thermally-driven boundary, $r = 1/2$. Thermal transport can be accurately predicted by the inner-outer matching problem formulated in the previous section, a key improvement over the ODE model [33] which does not resolve the boundary-layer and incorrectly predicts Nu to saturate to a constant at high Ra .

VII. DISCUSSIONS

In this manuscript we have extended the ODE model developed by Moore & Huang [33] for convection in an annulus to a new PDE model that fully resolves radial dependence of velocity and temperature fields while only retaining the lowest Fourier modes in the angular direction. The new PDE model takes the form of a reaction-diffusion system. While this new model fails to predict dynamic events, such as LSC reversals, it substantially improves the prediction of the time-averaged thermal transport. In particular, boundary-layer analysis of the new model predicts the scaling relationship $Nu \propto Ra^{1/4}$, which is confirmed by direct numerical simulation of the governing Navier-Stokes-Boussinesq equations.

We note that the $Nu \propto Ra^{1/4}$ scaling does not hold for every geometry. For example, extensive studies of thermal convection in a rectangular domain have yielded the Grossmann-Lohse theory [11, 17, 18], which suggests the dependence between Nu and Ra to be more complicated than a simple power law. A power law of the form $Nu \propto Ra^\gamma$ may hold locally, but the exponent γ depends on Pr and the range of Ra under consideration. For example, for $Ra = 10^8$ and $Pr = 4$, similar to the values considered in our numerical simulations, the Grossmann-Lohse theory yields an exponent of $\gamma \approx 0.28$. Fundamental differences thus exist between the annular and rectangular geometries. In particular, the center obstruction in the annular geometry suppresses the bulk motion through the center of the domain that is present in rectangular convection. These are simply two different geometries available for examining the principles of thermal convection, neither one being inherently superior to the other. An advantage of the annular domain is that it enables one to examine the interplay of large-scale circulation and thermal boundary layers in isolation of other complicating effects, such as bulk motion through the center. In this geometry, we have shown that it is possible to develop a simple, first-principled theory yielding a scaling law $Nu \propto Ra^{1/4}$ that is unambiguously consistent with DNS. This clean theory may offer a stepping-stone for understanding thermal transport in other geometries where additional confounding effects arise.

A shortcoming of the new model is that by over-resolving the radial dependence compared to the angular dependence, the damping action of diffusion suppresses the LSC reversal events that were accurately captured by the cruder ODE model. This shortcoming may perhaps be overcome by including additional θ -modes in model, thereby increasing the number of coupled PDEs. How many additional modes must be included to recover the reversals is a question for near-future research. Alternatively, it might be possible to account for the higher-order modes through stochastic forcing, with the forcing term chosen judiciously to recover statistical features of the system. With these questions left for future research, the key finding of the current paper is that the resolution in the radial direction does properly recover time-averaged thermal transport. With the accurate description of diffusive transport, it is now viable to couple this convective model to interfaces that move in response such effects, such as objects melting or dissolving in convectively excited flows [38–41].

SUPPLEMENTAL MATERIAL

Supplementary movies are available at <https://math.nyu.edu/~jinzi/research/AnnularConvectionHeatTransfer/>.

-
- [1] R. Salmon, *Lectures on Geophysical Fluid Dynamics* (Oxford University Press, 1998).
 - [2] J.-Q. Zhong, D. Funfschilling, and G. Ahlers, Enhanced heat transport by turbulent two-phase Rayleigh-Bénard convection, *Phys. Rev. Lett.* **102**, 124501 (2009).
 - [3] J. A. Whitehead, Moving heaters as a model of continental drift, *Phys. Earth Planet. In.* **5**, 199 (1972).
 - [4] J. Zhang and A. Libchaber, Periodic boundary motion in thermal turbulence, *Phys. Rev. Lett.* **84**, 4361 (2000).
 - [5] J.-Q. Zhong and J. Zhang, Thermal convection with a freely moving top boundary, *Phys. Fluids* **17**, 115105 (2005).
 - [6] J. A. Whitehead and M. D. Behn, The continental drift convection cell, *Geophys. Res. Lett.* **42**, 4301 (2015).
 - [7] J. M. Huang, J.-Q. Zhong, J. Zhang, and L. Mertz, Stochastic dynamics of fluid–structure interaction in turbulent thermal convection, *J. Fluid Mech.* **854** (2018).
 - [8] T. D. de Wit, V. V. Krasnoselskikh, S. D. Bale, J. W. Bonnell, T. A. Bowen, C. H. K. Chen, C. Froment, K. Goetz, P. R. Harvey, V. K. Jagarlamudi, A. Larosa, R. J. MacDowall, D. M. Malaspina, W. H. Matthaeus, M. Pulupa, M. Velli, and P. L. Whittlesey, Switchbacks in the Near-Sun Magnetic Field: Long Memory and Impact on the Turbulence Cascade, *Astrophys. J. Suppl. Ser.* **246**, 39 (2020).
 - [9] M. McCurdy, N. J. Moore, and X. Wang, Predicting convection configurations in coupled fluid–porous systems, *Journal of Fluid Mechanics* **953**, A23 (2022).
 - [10] J. A. Whitehead, *Energy Flow and Earth* (Springer, 2024).
 - [11] G. Ahlers, S. Grossmann, and D. Lohse, Heat transfer and large scale dynamics in turbulent Rayleigh-Bénard convection, *Rev. Mod. Phys.* **81**, 503 (2009).
 - [12] J. J. Niemela, L. Skrbek, K. R. Sreenivasan, and R. J. Donnelly, Turbulent convection at very high Rayleigh numbers, *Nature* **404**, 837 (2000).
 - [13] D. Funfschilling, E. Brown, A. Nikolaenko, and G. Ahlers, Heat transport by turbulent Rayleigh-Bénard convection in cylindrical samples with aspect ratio one and larger, *J. Fluid Mech.* **536**, 145 (2005).
 - [14] C. H. B. Priestley, Convection from a large horizontal surface, *Aust. J. Phys.* **7**, 176 (1954).
 - [15] C. H. B. Priestley, *Turbulent transfer in the lower atmosphere* (University of Chicago Press, 1959).
 - [16] B. Castaing, G. Gunaratne, F. Heslot, L. Kadanoff, A. Libchaber, S. Thomae, X.-Z. Wu, S. Zaleski, and G. Zanetti, Scaling of hard thermal turbulence in Rayleigh-Bénard convection, *J. Fluid Mech.* **204**, 1 (1989).
 - [17] S. Grossmann and D. Lohse, Scaling in thermal convection: a unifying theory, *J. Fluid Mech.* **407**, 27 (2000).
 - [18] R. J. A. M. Stevens, E. P. van der Poel, S. Grossmann, and D. Lohse, The unifying theory of scaling in thermal convection: the updated prefactors, *J. Fluid Mech.* **730**, 295 (2013).
 - [19] F. F. Araujo, S. Grossmann, and D. Lohse, Wind Reversals in Turbulent Rayleigh-Bénard Convection, *Phys. Rev. Lett.* **95**, 084502 (2005).
 - [20] E. Brown, A. Nikolaenko, and G. Ahlers, Reorientation of the large-scale circulation in turbulent Rayleigh-Bénard convection, *Phys. Rev. Lett.* **95**, 084503 (2005).
 - [21] H. F. Creveling, J. F. D. Paz, J. Y. Baladi, and R. J. Schoenhals, Stability characteristics of a single-phase free convection loop, *J. Fluid Mech.* **67**, 65 (1975).
 - [22] M. Gorman, P. J. Widmann, and K. A. Robbins, Chaotic flow regimes in a convection loop, *Phys. Rev. Lett.* **52**, 2241 (1984).
 - [23] M. Gorman, P. J. Widmann, and K. A. Robbins, Nonlinear dynamics of a convection loop: a quantitative comparison of experiment with theory, *Physica D* **19**, 255 (1986).
 - [24] E. Brown and G. Ahlers, Large-scale circulation model for turbulent Rayleigh-Bénard convection, *Phys. Rev. Lett.* **98**, 134501 (2007).
 - [25] H.-D. Xi and K.-Q. Xia, Cessations and reversals of the large-scale circulation in turbulent thermal convection, *Phys. Rev. E* **75**, 066307 (2007).

- [26] K. Sugiyama, R. Ni, R. J. A. M. Stevens, T. S. Chan, S.-Q. Zhou, H.-D. Xi, C. Sun, S. Grossmann, K.-Q. Xia, and D. Lohse, Flow reversals in thermally driven turbulence, *Phys. Rev. Lett.* **105**, 034503 (2010).
- [27] H. Song, E. Villermaux, and P. Tong, Coherent oscillations of turbulent Rayleigh-Bénard convection in a thin vertical disk, *Phys. Rev. Lett.* **106**, 184504 (2011).
- [28] Y. Wang, P.-Y. Lai, H. Song, and P. Tong, Mechanism of large-scale flow reversals in turbulent thermal convection, *Sci. Adv.* **4**, 7480 (2018).
- [29] X. Chen, S.-D. Huang, K.-Q. Xia, and H.-D. Xi, Emergence of substructures inside the large-scale circulation induces transition in flow reversals in turbulent thermal convection, *J. Fluid Mech.* **877**, R1 (2019).
- [30] A. Xu, X. Chen, and H.-D. Xi, Tristable flow states and reversal of the large-scale circulation in two-dimensional circular convection cells, *J. Fluid Mech.* **910**, A33 (2021).
- [31] E. N. Lorenz, Deterministic nonperiodic flow, *J. Atmos. Sci.* **20**, 130 (1963).
- [32] R. Ni, S.-D. Huang, and K.-Q. Xia, Reversals of the large-scale circulation in quasi-2D Rayleigh-Bénard convection, *J. Fluid Mech.* **778**, R5 (2015).
- [33] N. J. Moore and J. M. Huang, Large-scale circulation reversals explained by pendulum correspondence, *J. Fluid Mech.* **993**, A3 (2024).
- [34] R. Peyret, *Spectral methods for incompressible viscous flow*, Vol. 148 (Springer Science & Business Media, 2002).
- [35] J. M. Huang, M. J. Shelley, and D. B. Stein, A stable and accurate scheme for solving the Stefan problem coupled with natural convection using the Immersed Boundary Smooth Extension method, *J. Comput. Phys.* **432**, 110162 (2021).
- [36] J. M. Huang and J. Zhang, Rayleigh-Bénard thermal convection perturbed by a horizontal heat flux, *J. Fluid Mech.* **954**, 10.1017/jfm.2022.1035 (2022).
- [37] L. N. Trefethen, *Spectral methods in MATLAB* (SIAM, 2000).
- [38] J. M. Huang, M. N. J. Moore, and L. Ristroph, Shape dynamics and scaling laws for a body dissolving in fluid flow, *J. Fluid Mech.* **765**, 10.1017/jfm.2014.718 (2015).
- [39] M. N. J. Moore, Riemann-Hilbert Problems for the Shapes Formed by Bodies Dissolving, Melting, and Eroding in Fluid Flows, *Commun. Pure Appl. Math.* **70**, 1810 (2017).
- [40] S. Weady, J. Tong, A. Zidovska, and L. Ristroph, Anomalous Convective Flows Carve Pinnacles and Scallop in Melting Ice, *Phys. Rev. Lett.* **128**, 044502 (2022).
- [41] J. M. Huang and N. J. Moore, Morphological attractors in natural convective dissolution, *Phys. Rev. Lett.* **128**, 024501 (2022).